Dalton Transactions

ROYAL SOCIETY OF CHEMISTRY

PAPER

View Article Online
View Journal | View Issue

Cite this: *Dalton Trans.*, 2024, **53**, 5089

Chiral Au(III) chelates exhibit unique NCI-60 cytotoxicity profiles and interactions with human serum albumin†

Sheldon Sookai, *[a] Matthew P. Akerman [b] and Orde Q. Munro *[a,c]

Au(III) bis(pyrrolide-imine) chelates are emerging as a class of versatile, efficacious metallodrug candidates. Here, we synthesised two enantiopure chiral ligands **H_2L1** and **H_2L2** (tetradentate cyclohexane-1,2-diamine-bridged bis(pyrrole-imine) derivatives). Metallation of the ligands with Au(III) afforded the chiral cationic complexes **AuL1** and **AuL2**. The *in vitro* cytotoxicities of **AuL1** and **AuL2** determined in the NCI-60 single-dose drug screen were 56.5% and 89.1%, respectively. **AuL1** was subsequently selected for a five-dose NCI-60 screen, attaining GI_{50}, IC_{50}, and LC_{50} values of 4.7, 9.3 and 39.8 μM, respectively. Hierarchical cluster analysis of the NCI-60 data indicated that the profile for **AuL1** was similar to that of vinblastine sulfate, a microtubule-targeting vinca alkaloid. Reactions of **AuL1** with glutathione (GSH) *in vitro* confirmed its susceptibility to reduction, Au(III) → Au(I), by intracellular thiols. Because human serum albumin (HSA) is responsible for transporting clinically deployed and investigational drugs, we studied the uptake of **AuL1** and **AuL2** by HSA to delineate how chirality impacts their protein-binding affinity. Steady-state fluorescence quenching data acquired on the native protein and data from site-specific probes showed that the compounds bind at sites close enough to Trp-214 (subdomain IIA) of HSA to quench the fluorophore. The bimolecular quenching rate constants, K_q, were *ca.* 10^2 times higher than the maximum diffusion-controlled collision constant of a biomolecule in water (10^{10} M^{-1} s^{-1}), confirming that static fluorescence quenching was the dominant mechanism. The Stern–Volmer constants, K_{SV}, were ~10^4 M^{-1} at 37 °C, while the affinity constants, K_a (37 °C), measured ~2.1 × 10^4 M^{-1} (**AuL1**) and ~1.2 × 10^4 M^{-1} (**AuL2**) for enthalpy-driven ligand uptake targeting Sudlow's site I. Although far- and near-UV CD spectroscopy indicated that both complexes minimally perturb the secondary and tertiary structure of HSA, substantial shifts in the CD spectra were recorded for both protein-bound ligands. This study highlights the role of chirality in determining the cytotoxicity profiles and protein binding behaviour of enantiomeric Au(III) chelates.

Received 1st December 2023,
Accepted 8th February 2024

DOI: 10.1039/d3dt04024k

rsc.li/dalton

Introduction

Cancer accounted for almost 10 million deaths in 2020, and the rate is expected to continue to rise.[1] The fight against cancer is, unfortunately, becoming increasingly difficult due to drug resistance coupled with severe side effects from many currently deployed chemotherapy drugs. Since most statutory chemotherapeutic agents are organic, any metallodrugs progressing through Phase III human trials could become genuinely helpful next-generation chemotherapeutic agents. However, metallodrugs are underrepresented in pre-clinical screens and clinical trials compared with organic compounds, suggesting that most of their potential remains untapped.[2] The marked potential of metallodrugs was recently highlighted by an antibiotic screening centre, demonstrating that metallodrugs displayed a 10-fold higher hit rate towards ESKAPE pathogens than purely organic compounds.[3]

In 1965[4] it was first reported that cisplatin inhibited mitosis of bacteria; the ensuing clinical deployment of cisplatin and its analogues[5,6] as anti-cancer metallodrugs[7] ushered in an era of expansionary multidisciplinary studies on Pt(II) complexes[8] spanning several decades. Unfortunately, numerous cisplatin-resistant tumour cell lines have since emerged,[9,10] fuelling increased interest in metallodrug development, especially of isoelectronic (d^8) square-planar Au(III) complexes.[11–16]

[a]*Molecular Sciences Institute, School of Chemistry, University of the Witwatersrand, PO WITS 2050, Johannesburg, South Africa. E-mail: sheldon.sookai@wits.ac.za, orde.munro@leeds.ac.uk*
[b]*School of Chemistry and Physics, University of KwaZulu-Natal, Pietermaritzburg, 3201, South Africa*
[c]*School of Chemistry, University of Leeds, Woodhouse Lane, Leeds LS2 9JT, UK*

†Electronic supplementary information (ESI) available: Complete experimental details and supplementary tables and figures in PDF format, X-ray crystal structures in CIF format. CCDC 2244592 and 2244999. For ESI and crystallographic data in CIF or other electronic format see DOI: **https://doi.org/10.1039/d3dt04024k**

Au(III) complexes were originally believed to be mechanistically similar to Pt(II) compounds in biological systems. However, this is not the case, as the Au(III) ion is susceptible to reduction to either Au(I) or colloidal gold, *i.e.*, Au(0).[17] Therefore, it is crucial to identify appropriate multidentate ligands capable of stabilising Au(III) under physiological conditions.[18,19] Typical multidentate ligand scaffolds used to stabilise the Au(III) ion are porphyrins,[20] CNC-type pincer ligands,[13,14,21,22] and deprotonated pyrroles.[12] These ligands contain strong neutral or anionic σ-donor atoms (C, N, and O) to complement the hard Au(III) ion. The strong σ-donors within the scaffold transfer electron density toward the metal centre, lowering its reduction potential.[23]

Pyrrole-based ligands are essential building blocks for various organic pharmaceuticals,[24] as epitomised by clinically approved drugs, including Tolmetin (a non-steroidal anti-inflammatory agent),[25] Glimepiride (used to manage type-2 diabetes mellitus by stimulating insulin release),[26] and Sunitinib (multi-targeted receptor tyrosine kinase inhibitor for cancer chemotherapy).[27] Of relevance here, pyrrole-imine metal chelates exhibit significant medicinal potential. The best-known example is the pentadentate macrocycle texaphyrin,[28] which complexes Lu(III)[29] and is a promising, though not FDA-approved, candidate for photodynamic therapy.[30] Despite being further behind on the clinical development trajectory, patented tetradentate bis(pyrrolide-imine) chelates of Au(III) are promising investigational compounds for cancer[12] and mycobacterial chemotherapy.[31]

Regarding anti-cancer Au(III) complexes, limited work has been published on assessing their binding potential to serum proteins, in particular human serum albumin (HSA), which can play an essential role in determining plasma distribution, pharmacokinetic and pharmacodynamic data of metallodrugs.[32] HSA is the most abundant serum protein existing at physiological concentrations of around 600 μM.[33] The critical roles of HSA are to transport both endogenous and exogenous compounds and regulate colloidal osmotic pressure. As illustrated in Scheme 1, HSA is a single polypeptide chain consisting of three domains, namely I (residues 1–195), II (196–383), and III (384–585), that are further broken down into two subdomains A and B.[34,35] HSA has several binding sites that bind exogenous and endogenous compounds: (i) two primary drug binding sites named Sudlow's site I and II, (ii) four thyroxine sites, (iii) seven fatty acid sites, and (iv) several known metal ion binding sites.[36] Given the abundance and function of HSA as a blood plasma transporter, delineating the binding of a medicinal compound to HSA is central to understanding the pharmacodynamic and pharmacokinetic data of the compound *in vivo*.[37]

In this study, we synthesised the Au(III) chelates N,N′-(1*S*,2*S*)- and N,N′-(1*R*,2*R*)-cyclohexane-1,2-diylbis[nitrilo(*E*)methylylidene]bis(pyrrol-1-ido) Au(III) hexafluorophosphate(V), which we have abbreviated [Au((1*S*,2*S*)**L1**)]PF_6 (**AuL1**) and [Au((1*R*,2*R*)**L2**)]PF_6 (**AuL2**), respectively (Scheme 2). An NCI-60 screen[38] was used to gauge the cytotoxicity of both Au(III) chelates. Significantly, **AuL1** (but not **AuL2**) was sufficiently active to warrant full five-dose screening. Spectroscopic methods

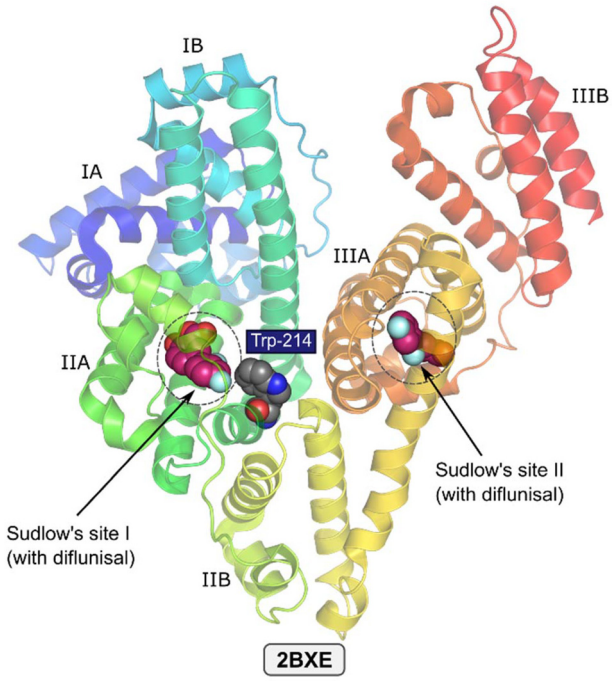

Scheme 1 X-ray structure of HSA bound to diflunisal (redrawn from PDB code 2BXE) illustrating the two primary small molecule binding sites. Sudlow's site I is larger than Sudlow's site II, and compounds that bind in this pocket perturb the fluorescence of Trp-214 strongly. The protein secondary structure elements are depicted schematically, coloured by domain, and labelled. A third diflunisal molecule bound centrally in domain IIB has been omitted for clarity.

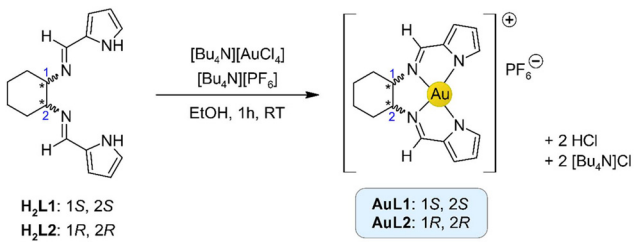

Scheme 2 Synthetic route depicting the metalation of H_2**L1** and H_2**L2** with Au(III).

were used to probe (i) the redox stability (GSH reactivity assays) and (ii) the binding of **AuL1** and **AuL2** to HSA under physiological conditions. Notably, **AuL1** interacted somewhat more tightly with HSA relative to its enantiomer, highlighting how the chirality of the metal complex influences its uptake by the transporter protein.

Results and discussion

Metal chelate synthesis

Au(III) chelates **AuL1** and **AuL2** were synthesised by the method described in Scheme 2. The enantiopure bis(pyrrole-imine) Schiff base ligands (1*S*,2*S* and 1*R*,2*R* enantiomers) were specifi-

cally employed for their chirality and ability to stabilise a high oxidation state metal ion such as Au(III). The pyrrole nitrogen atoms are concomitantly deprotonated upon metalation in this reaction, affording the desired chiral cationic Au(III) chelates. Interestingly, **AuL1** and **AuL2** only precipitated when $[Bu_4N][PF_6]$ was added to the reaction mixture. This is attributed to switching the Cl^- counterion to PF_6^-, which presumably lowers the solubility product of the salt by better ion pair formation.

X-ray crystal structures of enantiomeric AuL1 and AuL2

The structures of **AuL1** and **AuL2** were elucidated by single crystal X-ray diffraction (Fig. 1, Fig. S30–S32, and Tables S2–S7†). **AuL1** and **AuL2** crystallised in the chiral space groups $P2_1$ (two independent molecules per asymmetric unit, ASU) and $P2_122_1$ (two independent half molecules per ASU), respectively. The Au(III) chelates exhibit the expected four-coordinate square planar geometry (Fig. 1 and S30†) and are metrically similar enantiomers in terms of their general structural parameters

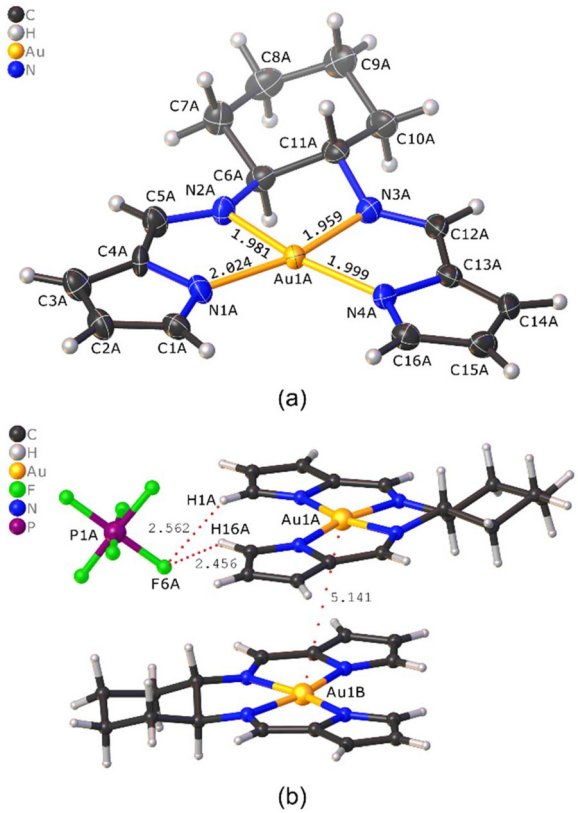

Fig. 1 (a) Labelled thermal ellipsoid view (50% probability surfaces) of the X-ray structure of $[AuL1]^+$ belonging to independent cation A of the asymmetric unit (ASU). The PF_6^- counterion and second independent ion pair are omitted for clarity (H atoms are shown as spheres with an arbitrary radius). Selected bond distances are in Å units. (b) Stacking of independent cations A and B in the ASU; the cations have no close contacts. The long Au···Au distance of 5.1409(3) Å indicates an insignificant metal-to-metal interaction. One of two types of noncovalent F···H–C (pyrrole) interactions between PF_6^- and $[AuL1]^+$ in the crystal lattice of the salt is illustrated.

such as Au–N bond lengths and bond angles subtended at the metal centre (Fig. S32 and Table S8†). For brevity, only the structure of **AuL1** will be discussed further, given the slightly higher quality X-ray data set for this compound, its higher cytotoxicity in the NCI-60 screens, and its higher affinity for HSA (*vide infra*).

The $Au–N_{imine}$ bond distances average 1.975(11) Å, which is ~2% shorter than the $Au–N_{pyrrole}$ distances (2.012(16) Å). Regarding Au(III) complexes containing $Au–N_{pyrrole}$ and $Au–N_{imine}$ bonds, **AuL1** is unique in the sense that its $Au–N_{imine}$ bonds are notably shorter than the $Au–N_{pyrrole}$ bonds. This reflects the structural constraints imposed by the central 5-membered chelate ring (*i.e.*, the chiral cyclohexyl bridge). When compared with the Au–N bond distances for the related Au(III) complexes bearing 3- or 4-carbon aliphatic chains linking the imine nitrogen atoms,[12] the $Au–N_{pyrrole}$ bond length in **AuL1** is ~1% longer and the $Au–N_{imine}$ bond length ~1.5% shorter than those of the achiral congeners. Overall, the observed Au–N bond distances for **AuL1** are comparable to previously reported Au–N bond distances, which range from 1.928–2.216 Å.[39] Regarding the coordination group bond angles for **AuL1**, the mean $N_{pyrrole}–Au–N_{pyrrole}$ bond angle (112.8 ± 0.1°) is 14.4% wider and the mean $N_{imine}–Au–N_{imine}$ bond angle (84.4 ± 4°) 13.5% more acute compared with those reported by Akerman *et al.*[12] for the structurally-related achiral analogues. This again reflects the 2-carbon chain of the cyclohexyl ring linking the imine groups of **AuL1**, a structural scaffold which clearly sterically strains the tetradentate chelate, substantially widening and narrowing the $N_{pyrrole}–Au–N_{pyrrole}$ and $N_{imine}–Au–N_{imine}$ bond angles, respectively. In short, the Au–N bond distances in **AuL1** hinge mainly on the central chelate ring's bite angle.

Considering the extended structure of **AuL1**, the only short contacts present involve the PF_6^- counterion, leading to F···H–C(pyrrole) intermolecular interactions which stabilise the crystal lattice (Fig. 1b). F···H–C nonbonded interactions are known;[40] although they seldom form strong H-bonds due to electrostatic and steric factors,[41] their role in molecular packing cannot be ignored. The **AuL1** cations and PF_6^- anions display measurable F···H–C(pyrrole) contacts, with distances ranging from 2.456–2.726 Å (Fig. 1b). The structural role played by fluorine is perhaps further highlighted by the fact that crystallisation of **AuL1** was only possible with PF_6^- as the counterion, not Cl^-. As shown in Fig. 1, the **AuL1** cations deviate negligibly from planarity; only the atoms of the cyclohexyl groups lie out of the mean plane defined by the Au(III) ion and pyrrole-imine chelates. Any minor out-of-plane deviations may be attributed to the twist induced by the cyclohexyl bridging group of the ligand rather than packing interactions. Notably, there were no aurophilic Au···Au contacts between neighbouring cations since the atomic separation exceeded 5 Å for both **AuL1** and **AuL2** (Fig. 1 and S32†). For both **AuL1** and **AuL2**, the cation pairs exhibit nonbonded contacts between the Au(III) ions and pyrrole β-C atoms, with those of **AuL2** (3.272 and 3.315 Å) being shorter than the sum of the crystallographic van der Waals radii of carbon and gold (3.80 Å).[42]

NCI-60 cytotoxicity screens

To evaluate the anticancer potential of **AuL1** and **AuL2**, both compounds were subjected to single-dose NCI-60 cytotoxicity screens (10 μM test agent concentration; National Cancer Institute, Bethesda, MD). Both **AuL1** and **AuL2** were active, affording dissimilar mean growth percentages of 56.5% and 89.1%, respectively, thereby reflecting an enantiomer-dependent response. Since **AuL1** was the more active of the two Au(III) chelates, it was selected for a full NCI-60 five-dose screen, spanning the concentration range 10^{-8}–10^{-4} M. The cytotoxicity data for **AuL1** and **AuL2** are available in the ESI.†

From the five-dose screen of **AuL1**, the lowest IC_{50} values were for most of the ovarian cancer cell lines, the non-small lung cancer cell line NCI-522 (2 μM), the colon cancer cell line SW-620 (2.57 μM), and the OVCAR-3 cell line (2.95 μM). Fig. 2 compares the best GI_{50} values for **AuL1** with analogous data for clinically deployed anti-cancer therapeutics that have a definitive mode of action (MOA). Mean cytotoxicity parameters for **AuL1** obtained for each of the nine classes of human cancer in the NCI-60 screen are listed in Fig. S26.† Collectively, the data indicate that Leukaemia and melanoma cancer cell lines are, on average, the most susceptible to the Au(III) complex with GI_{50} and IC_{50} values below 10 and 20 μM, respectively.

Assessment of the cytotoxicity data in Fig. 2 and Table 1 for **AuL1** is illuminating. Specifically, the GI_{50} value for **AuL1** is not as low as that of commercial anti-cancer therapeutics. However, the IC_{50} and LC_{50} values are lower than both cisplatin and carboplatin and are within the range of mitomycin. From Fig. 2, the steepness of the curve indicates that the initial concentration of **AuL1** necessary to induce cell death is high compared to the commercially available drugs. However, once this concentration has been reached, relatively low increases in **AuL1** concentration lead to high levels of cell mortality. Comparison of **AuL1** with camptothecin, a powerful topoisomerase I poison, highlights the observation.

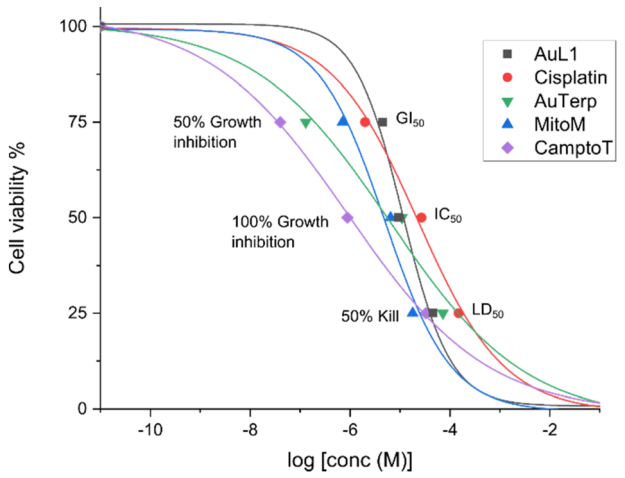

Fig. 2 Mean NCI-60 GI_{50}, IC_{50} and LC_{50} curves for three commercial anti-cancer agents (cisplatin, mitomycin, MitoM, and camptothecin, CamptoT), Au(III)–terpyridine (AuTerp) and **AuL1** (synthesised in this work). Data were obtained from the DTP drug respiratory data base.[43]

Table 1 Summary of the average cytotoxicity data over 60 human cancer cell lines for **AuL1** and selected commercial cytotoxic agents for comparison

Drug	GI_{50} (μM)	IC_{50} (μM)	LC_{50} (μM)
AuL1	4.7	9.3	39.8
Cisplatin	2.0	27	>100
Carboplatin	99.6	>100	>100
$[Au^{3+}(terpy)Cl]Cl_2$	0.13	11	73
Mitomycin	0.71	6.5	18
Camptothecin	0.040	0.89	33

For 50% growth inhibition (a 25% cell mortality rate), on average, a concentration of 4.7 μM of **AuL1** is required. To induce 75% cell death (LC_{50}), only an 8-fold increase in concentration is needed, *i.e.*, [**AuL1**] = 39.8 μM. For camptothecin to induce the same results, an increase in concentration of 825-fold is required, *i.e.*, from 0.040 μM to 33 μM. These numbers illustrate the difference in the steepness of the dose–response curves (Fig. 2). It is important to note that a commercially successful anti-cancer compound does not need to rely only on GI_{50} values. An example is 5-fluorouracil which displays only moderate cytotoxicity (for many cell lines, the GI_{50} exceeds 10 μM); however, the drug is a widely prescribed antineoplastic antimetabolite.[44]

Despite the reduced toxicity of **AuL1** compared to taxol and daunorubicin, **AuL1** is still more active than cisplatin, 5-fluorouracil and mitomycin in many cases. Therefore, it exhibits sufficient cytotoxicity to be considered as a metallodrug candidate with chemotherapeutic potential for treating several tumour cell lines, particularly leukaemias. Notably, despite the significant cytotoxicity of drugs such as taxol and daunorubicin, these drugs are often not the first choice of oncologists for the treatment of various tumours.[45,46] This is because these and other drugs, particularly strong DNA alkylating agents, have been implicated in the onset of secondary cancers,[45,46] usually leukaemias, associated with the initial treatment of solid tumours during childhood.[47]

Why is the 1*S*,2*S* (AuL1) enantiomer more active than the 1*R*,2*R* (AuL2)?

Both **AuL1** and **AuL2** are chiral molecules, with **AuL1** being the more active enantiomer. The effect of chirality is well understood in drug design.[48] A probable reason for **AuL1** being more active than **AuL2** is that most proteins in the cellular environment are said to be "left-handed" since they are made up of primarily L-enantiomer amino acids.[49] It would appear that the (1*S*,2*S*)-enantiomer interacts more favourably with its cellular target(s) within this lefthanded environment. It is well known that enzymes react specifically with certain substrates, and it is now believed that many drug receptors are similarly more accessible to specific enantiomers.[49] Accordingly, the efficacy of one enantiomer is often heightened over the opposite enantiomer.[49,50]

For the current compounds, the (1*R*,2*R*)-enantiomer evidently binds less strongly to one or more drug target sites (which are currently unknown), culminating in diminished cytotoxicity relative to the (1*S*,2*S*)-enantiomer. A second factor is that cellular uptake and metabolism of the (1*S*,2*S*)-enantiomer could be intrinsically higher, particularly if active transport is involved, thus inducing a greater therapeutic/cellular effect.[48] An assessment of the relative cellular distribution of elemental gold after the uptake of **AuL1** and **AuL2** might be illuminating in this regard. Significantly, a difference in the rate of metabolism has been shown previously to affect the efficacy of one enantiomer over another.[49] In this work, each enantiomer was screened separately against a panel of human cancer cell lines. In many cases, drugs are administered as a racemate with equal efficacy.[48–50] Going forward, it may be worth studying the cytotoxicity of a racemic mixture of **AuL1** and **AuL2**, which would be considerably more cost-effective to produce, as a synergistic cytotoxic effect is possible in principle. Any further development thereafter would hinge on an assessment of the toxicology and metabolism of each enantiomer.[49]

Similarity of AuL1 to commercially available drugs

Our cell screening data has shown that **AuL1** is an anticancer agent with sufficient potential. Determining the mechanism of action for **AuL1** is the next critical step towards its possible development as a chemotherapeutic agent. Knowledge of the mode of action of many chemotherapeutic agents is scant, particularly metal-based compounds. Therefore, determining the specific mode of action of **AuL1** will be critical.

Regarding the NCI-60 screen for **AuL1**, 180 data points are generated from the GI_{50}, IC_{50} and LC_{50} values in a full 5-dose screen. This quantity of data enables an accurate statistical comparison of the cytotoxicity profile for **AuL1** with compounds in the NCI-60 database that have an established mechanism of action. Using the NCI-60 data for **AuL1** and 21 FDA-approved drugs, hierarchical cluster analysis indicated that the cytotoxicity profile of **AuL1** is strongly correlated with vinblastine sulphate (Fig. 3). Vinblastine sulphate is an anti-microtubule drug similar to taxol[51] which inhibits mitosis by binding to the microtubular proteins of the mitotic spindle. Notably, **AuL1** also clustered, albeit more distantly, with daunorubicin, cisplatin and thiopurine, suggesting the Au(III) chelate likely targets proteins that interact with DNA in a chromatin setting. The statistical data do not, however, confirm the mechanism of action of **AuL1**, but suggest which protein targets should be investigated in inhibition assays going forward. One caveat is that **AuL1** may function as a prodrug (due to potential reduction of the metal ion), which would complicate interpretation of the data and identification of the cellular target(s).

Reaction of AuL1 with GSH – postulated mechanism of action

DNA serves as a conventional biological target for metallodrugs, including the Au(III) chelates in this study, which were initially proposed for their potential to bind to and intercalate

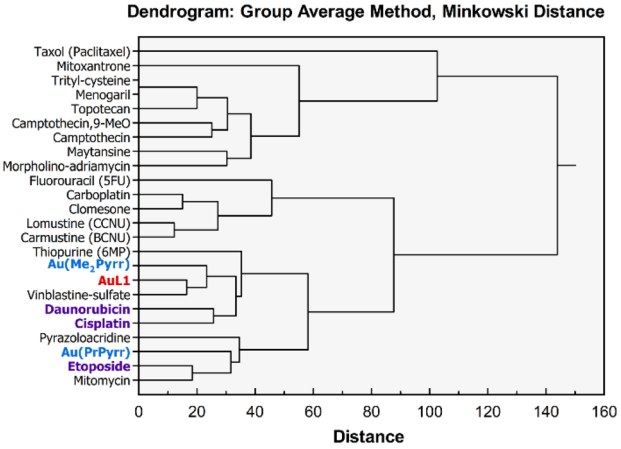

Fig. 3 Comparison of the activity profile of commercial drugs with a known mode of action, the previously patented Au(Me_2Pyrr) and Au(PrPyrr),[52] and **AuL1** synthesised in this work.

with DNA. The poor binding affinity of **AuL1** and **AuL2** for calf thymus DNA (ctDNA), however, indicates the involvement of alternative biological targets (Fig. S34†). Several studies indicate that Au(III) complexes undergo facile reduction to Au(I) or Au(0) by intracellular thiols. Given the presence of glutathione (GSH) in cancer cells with concentrations ranging from 0.5–10 mM,[53] we analyzed the stability of **AuL1** in the presence of varying GSH concentrations (Fig. S33†).

The reaction between **AuL1** and GSH was monitored over time through electronic spectroscopy in the UV-visible region, utilising a 1 : 1 mole ratio (**AuL1** : GSH) of the reactants, as depicted in Fig. S33a.† Spectral changes in Fig. S33a† reveal that **AuL1** (100 μM) in the presence of GSH (100 μM) leads to a decrease in the intensity of the $\pi \rightarrow \sigma^*$ band of **AuL1** at 380 nm, accompanied by a corresponding increase in the intensity of the $\pi \rightarrow \pi^*$ band at 290 nm. These spectral variations reflect the anticipated changes during reduction of the Au(III) chelate. However, after 5 hours, no further spectral changes were observed, likely due to the complete oxidation of GSH. Subsequently, the reaction was monitored over time using a 1 : 10 mole ratio (**AuL1** : GSH) of the two reactants, as presented in Fig. S33b.† After 15 minutes, a rapid reduction of Au(III) to Au(I) was noted, possibly accompanied by the dissociation of the pyrrole and imine motifs from the metal ion centre. During the reduction of Au(III), an initial blue shift of 15 nm (attributed to the hydrolysis of the Au–N bond of the coordinated pyrrole ring)[54] is observed, followed by the emergence of a peak at 320 nm (likely Au(I)) and the disappearance of the 380 nm maxima.

The reduction of Au(III) to Au(I) is not uncommon in Au(III) complexes, and this phenomenon is attributed to their limited stability under physiological conditions. Surprisingly, this fundamental aspect is often overlooked, particularly in work on Au(III)–NHCs (NHC, N-heterocyclic carbene) and their mode of action.[55–58] Despite the deliberate use of ligands known for their robust σ-donating and π-accepting properties,[59] *i.e.*, nor-

mally capable of stabilising Au(III), our findings indicate that the present Schiff base ligands do not thwart redox reactions. Based on the reduction of **AuL1** and **AuL2** by GSH, we tentatively conclude that the cytotoxic mode of action of both Au(III) chelates may involve as yet unidentified species derived from reduction of the complexes after cell uptake. In short, **AuL1** and **AuL2** could be prodrugs.

The Au(I) ion, characterised as a soft metal ion, exhibits a notable affinity for soft Lewis bases, particularly thiols.[60] Consequently, thiol-containing enzymes, such as thioredoxin reductase (TrxR), glutathione reductase (GR), or cysteine protease, are likely targets for an Au(I) species derived from **AuL1**. These proteins, often overexpressed in cancer cells,[61–63] emerge as potential candidates for anti-cancer therapy involving Au complexes. Both GR and TrxR play essential roles in the redox regulation of vital cellular processes. These processes include cell growth, DNA transcription and synthesis, and drug resistance.[64,65] If reductive demetallation of Au(III) to Au(I) occurs for **AuL1** after cell uptake, the reduced species could potentially function as a disulfide reductase inhibitor.[61] Mechanistically, this would involve Au(I) coordination by cysteinyl residues within the active site of either GR or TrxR. This concept finds support in prior studies by Becker *et al.*,[63] where XRD analysis demonstrated linear coordination of an Au(I) phosphine complex to the active site of human disulfide reductases, forming a "$S_{cysteine}$–Au(I)–phosphine" adduct. Similar observations are reported with auranofin interacting with thioredoxin-glutathione reductase[66] and trypanothione reductase, a disulfide reductase.[67] Speculation aside, our future work aims to address the ultimate cellular fate of **AuL1** by investigating its reactions with these target proteins.

Can AuL1 and AuL2 bind as intact metal chelates to HSA?

The interaction of potential pharmaceutical compounds (**AuL1** and **AuL2** in this study) with plasma proteins is crucial in determining their bioavailability.[68] When evaluating potential therapeutic agents, thoroughly examining plasma protein binding becomes imperative. Of particular importance is the interaction of the compounds with HSA, a vital serum transport protein within the circulatory system. HSA binds a diverse array of both endogenous metabolic compounds and exogenous therapeutic pharmaceuticals.[37]

The binding of a drug to HSA significantly impacts the free drug concentration, thereby influencing its bioavailability *in vivo*. HSA can function as a reservoir for therapeutic agents, enhancing accessibility at concentrations surpassing their plasma solubility, or it may act as a rapid clearance route, potentially impeding the compound's ability to exert its therapeutic effect. These outcomes can be inferred from the compound's binding affinity to the protein.[69–71] In the case of a drug exhibiting high binding affinity to HSA, there is a resultant decrease in free drug concentrations, leading to an increased drug half-life, as the bound fraction is less susceptible to metabolic processes in the liver.[69] Consequently, investigating the binding of a prospective drug to HSA represents a crucial initial step in elucidating the pharmacokinetics and pharmacodynamics of the compound, offering valuable insights into its potential therapeutic efficacy.[37] Here, we investigated several biophysical parameters for the binding of the present chiral Au(III) chelates to HSA using diverse spectroscopic methods (*vide infra*). The key question we wanted to answer was whether **AuL1** and **AuL2** could be taken up by HSA as intact Au(III) complexes given their propensity for reduction with GSH, especially since HSA has a solvent-exposed cysteine residue (Cys-34). We also wished to understand whether uptake by HSA was enantiomer-dependent.

Fluorescence quenching measurements

When a small molecule binds to a protein in close proximity to an aromatic residue (Trp, Tyr and, to a lesser extent, Phe),[72,73] the intrinsic fluorescence of that protein will be disrupted.[73] The majority of HSA's fluorescence is attributed to Trp-214 in subdomain IIA. Importantly, Trp has a higher quantum yield and a more efficient resonance energy transfer than both Tyr and Phe.[74]

Quenching of the intrinsic emission spectrum of HSA (λ^{ex}, 295 nm) was investigated by titrating the protein with **AuL1** and **AuL2** over the concentration range 0–97 μM with spectral acquisition from 310–400 nm (Fig. 4). The λ^{em}_{max} was observed at ~342 nm in phosphate buffer, and the intrinsic emission intensity of HSA decreased monotonically with the addition of each aliquot of titrant (Fig. 4). The fluorescence quenching data indicate that both Au(III) chelates bind to HSA near enough to Trp-214 to alter its microenvironment, thereby quenching its fluorescence. The fluorescence quenching could be the result of different mechanisms, such as collisional

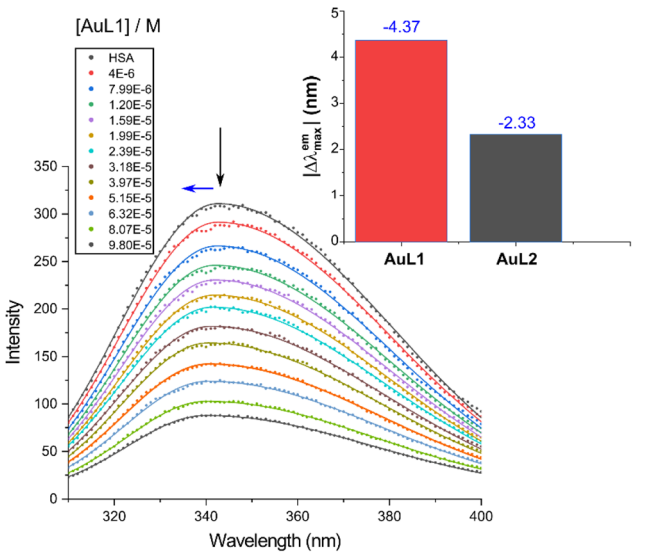

Fig. 4 Emission spectra of human serum albumin (HSA, 5.0 μM) recorded as a function of the concentration of **AuL1** at 298 K in KH_2PO_4 (50 mM, pH 7.50). Analogous spectra for the reaction of HSA with **AuL2** are given in Fig. S23 (ESI).† The absolute value of the wavelength shift accompanying ligand uptake ($|\Delta\lambda^{em}_{max}|$) is plotted as the inset to the main figure (upper right).

quenching, molecular rearrangements, energy transfer, or ground state complex formation.[75,76]

The binding of **AuL1** and **AuL2** to HSA is accompanied by blue shifts in λ_{max}^{em} of 4.37 and 2.33 nm, respectively. The λ_{max}^{em} shift data suggest that the Trp-214 residue is in a less polar environment after the uptake of both Au(III) chelates.[77,78] Two reasons might account for the λ_{max}^{em} blue shifts: (i) disruption of ordered water molecules that lie between 15–25 Å of Trp-214, which may cause orientation-dependent polarisation of the fluorophore, and/or (ii) direct electronic polarisation of the indole ring on the tryptophan residue by closely bound metal chelates. It is certainly feasible that binding of **AuL1** and **AuL2** by HSA both displaces ordered water molecules and induces some electronic polarisation of Trp-214, which affects the lowest energy $^1A_1 \rightarrow {}^1L_a$ ground state transition of Trp's indole ring,[77] thereby causing the λ_{max}^{em} shift. Ultimately, the different magnitudes of the measured λ_{max}^{em} shifts indicate that **AuL1** electronically perturbs Trp-214 more than **AuL2**. The different chirality of each metal chelate thus impacts the electronic structure of Trp-214, possibly because of differences in the way the metal chelates are positioned within the binding site.

Fluorescence quenching mechanism

Protein fluorescence quenching can be described mechanistically as either static, dynamic or a combination of both and is typically analysed using the Stern–Volmer equation (eqn (1)),[79]

$$I_0/I = 1 + K_{SV}[Q] = 1 + k_q\tau_0[Q] \quad (1)$$

where I_0 is the fluorescence intensity of HSA in the absence of the added quencher (Au(III) chelate herein), and I is the fluorescence intensity of HSA in the presence of the metal complex. K_{SV} is the Stern–Volmer constant (M^{-1}), while [Q] is the molar concentration of the quencher (*i.e.*, added **AuL1** or **AuL2**), k_q is the bimolecular quenching rate constant (M^{-1} s^{-1}), and τ_0 is the average lifetime of HSA fluorescence in the absence of any quencher (6.72 ± 0.07 ns,[74] 5.60 ± 0.10 ns,[80] and 5.28 ± 0.03 ns;[81] average = 5.87 ± 0.76 ns). Typically, the quenching mechanism can be differentiated by analysing the HSA···**AuL1/L2** complex's fluorescence as a function of temperature and viscosity.[82]

From least-squares fits of eqn (1) to the dose-dependence of I_0/I, the bimolecular fluorescence quenching rate constant for the HSA···Au(III) chelate interaction can easily be deduced from eqn (2), provided that τ_0 is known (*vide supra*).

$$k_q = \frac{K_{SV}}{\tau_0} \quad (2)$$

A linear Stern–Volmer plot is widely accepted to be associated with a single dominant quenching mechanism, either dynamic (diffusion-limited collisional) or static (binding-related).[79,83] The quenching mechanism can be differentiated by the temperature dependence of K_{SV}. When a static quenching mechanism is dominant, the K_{SV} value decreases with increasing temperature due to the decrease in the HSA-ligand formation constant. However, when a dynamic quenching mechanism is dominant, the K_{SV} values increase with increasing temperature due to an increase in the collisional frequency and diffusion rate.[84]

The Stern–Volmer plots for **AuL1** and **AuL2** (Fig. 5a) were both linear, suggesting a single class of quenching was dominant. In both cases, the K_{SV} values increased with increasing temperature, consistent with a dynamic quenching mechanism.[85] A summary of the K_{SV} and K_q values obtained for the interaction of **AuL1** and **AuL2** with HSA is given in Table 2. It is probable that the observed K_{SV} order, **AuL1** > **AuL2**, is due to the binding orientation of **AuL1** around Trp-214 (based on

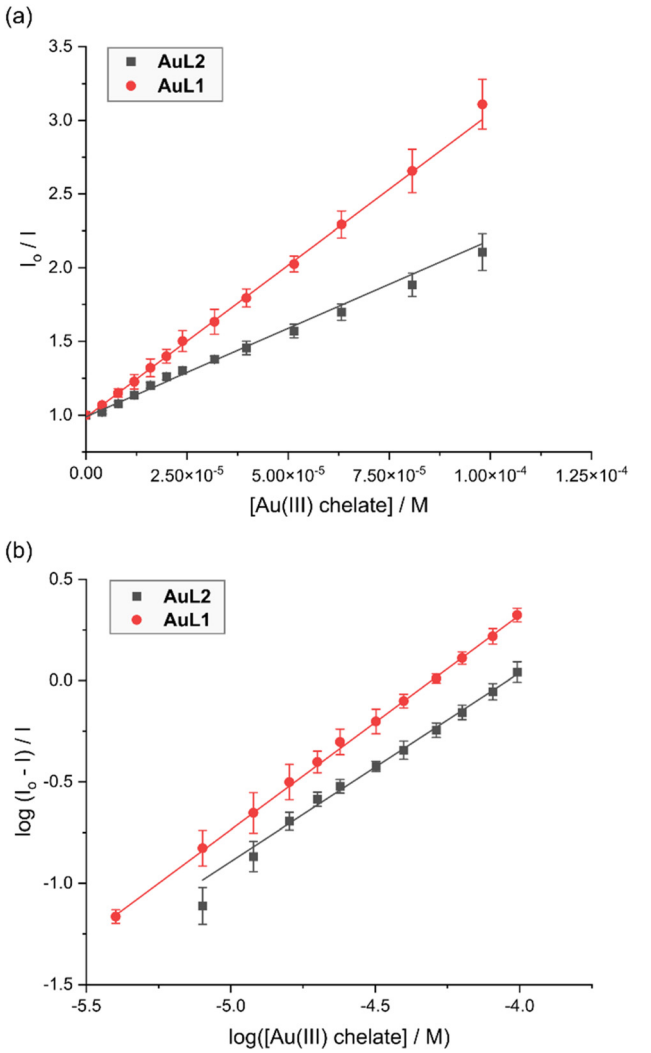

Fig. 5 (a) Stern–Volmer (SV) fluorescence intensity ratio plots for human serum albumin (HSA, 5.0 μM) recorded as a function of the concentration of **AuL1** and **AuL2** (50 mM KH_2PO_4, pH 7.50) at 37 °C. Error bars are ESDs based on the average of three independent determinations. The data are well-fitted by eqn (1) for linear SV emission behaviour. (b) Double logarithm plot of the fractional change in fluorescence intensity for human serum albumin (HSA, 5.0 μM) recorded as a function of the concentration of **AuL1** and **AuL2** (50 mM KH_2PO_4, pH 7.50) at 37 °C. Error bars are ESDs based on the average of three independent determinations. The data are described by eqn (3), which affords the affinity constant and stoichiometric coefficient for the reaction (Table 2).

Table 2 Stern–Volmer quenching constants (K_{SV}) and bimolecular quenching rate constants (k_q) for the interaction of **AuL1** and **AuL2** with HSA at different temperatures in 50 mM KH_2PO_4 buffer at pH 7.50

Cpd.	Temp. T (K)	10^{-5} K_{SV}[a,c] (M^{-1})	10^{-12} k_q[b] (M^{-1} s^{-1})	log(K_a/ M^{-1})[c]	n[d]
AuL1	288	1.19 (0.09)	2.03	4.93 (0.04)	1.17 (0.01)
	298	1.96 (0.01)	3.33	4.55 (0.02)	1.05 (0.01)
	310	2.55 (0.01)	4.35	4.32 (0.04)	0.98 (0.01)
AuL2	288	1.04 (0.01)	1.77	4.80 (0.01)	1.18 (0.01)
	298	1.11 (0.01)	1.89	4.33 (0.08)	1.06 (0.02)
	310	1.16 (0.01)	1.97	4.08 (0.05)	1.01 (0.01)

[a] K_{SV} values (Stern–Volmer constants) for the two Au(III) chelates were determined by fitting the data to eqn (1). [b] A mean excited state lifetime, τ_0, of 5.87(76) ns for HSA was used to calculate the bimolecular quenching rate constant, k_q. [c] The estimated standard deviation of the least significant digits are given in parentheses. [d] Ligand : HSA binding stoichiometry from the fit of the data to eqn (3).

Fig. 4). The bimolecular quenching rate constants (k_q) determined for **AuL1** and **AuL2** exceeded the diffusion-controlled limit (10^{10} M s^{-1})[85] by at least two orders of magnitude. These k_q values signal that the uptake of both Au(III) chelates by HSA is not randomised but consistent with a significant HSA···ligand binding interaction.

Binding affinity hinges on Au(III) chelate chirality

Quenching of HSA intrinsic fluorescence as a function of ligand dose, [**AuL*n***], can be used to calculate the binding affinity (K_a) and the stoichiometry (n). Both values can be delineated from a double log plot of the emission quenching data as a function of quencher (metal chelate) concentration, [Q] (eqn (3)),[86]

$$\log\left(\frac{I_0 - I}{I}\right) = \log K_a + n\log[Q] \quad (3)$$

where the intercept and slope of the curve give $\log K_a$ and n, respectively. The data for **AuL1** and **AuL2** are summarised in Table 2 and are plotted in Fig. 5b. Both compounds exhibit a moderate binding affinity for HSA (K_a ~10^5 M^{-1}), which is ideal for this study since we intend to show that HSA can serve as a transporter protein for this class of compounds. Importantly, it suggests that **AuL1** and **AuL2** could use the HSA-mediated cell entry pathway.[87] Binding constants that are too high will probably result in the retention of the compounds by HSA and thus diminished delivery *via* the HSA-mediated pathway.

From Table 2, the $\log K_a$ values differ by up to 0.24 log units at each temperature and follow the order **AuL1** > **AuL2**; the difference in chirality clearly impacts compound uptake by the protein, with the 1*S*,2*S* enantiomer being favoured. Such an outcome is not without precedent for drug enantiomers. For instance, the *S* enantiomer of warfarin has a higher binding constant than the *R* enantiomer.[88] Enantiomers can bind to the same region (binding site) or different regions depending on allosteric modulation.[89] Notably, the affinity constant data for **AuL1** and **AuL2** mirror the emission wavelength shifts induced by the binding of each Au(III) chelate to HSA (Fig. 4). The collective picture is that **AuL1** may bind closer to Trp-214 than **AuL2** or with an orientation that induces greater electronic perturbation of the fluorophore, and fit more snugly within the binding pocket, which is presumably Sudlow's site I (Scheme 1).

From Fig. 5b, it can be seen that the slopes of the double log plot linear fits were ~1 at 37 °C, strongly suggesting a 1 : 1 binding ratio of Au(III) chelate to HSA. For both chelates, $\log K_a$ decreases with increasing temperature, consistent with an exothermic reaction (*vide infra*).

Thermodynamics of Au(III) chelate binding hinge on chirality

$$\ln K_a = -\frac{\Delta H}{RT} + \frac{\Delta S}{R} \quad (4)$$

$$\Delta G = \Delta H - T\Delta S \quad (5)$$

Both **AuL1** and **AuL2** follow a linear van't Hoff relationship; plots for triplicate measurements are given in Fig. 6a. Under non-standard conditions, the entropy change (ΔS), enthalpy change (ΔH), and Gibbs free energy change (ΔG), may be gathered from the temperature dependence of the affinity constants (K_a) using eqn (4) and (5):

Table 3 summarises the thermodynamic parameters for the reaction of **AuL1** and **AuL2** with HSA in KH_2PO_4 buffer at neutral pH. Both reactions were exergonic,[86] with ΔG ranging from −25.5 kJ mol^{-1} for **AuL2** to −27.5 kJ mol^{-1} for **AuL1** at 298 K. As depicted graphically in Fig. 6b, the values of ΔG are remarkably similar due to enthalpy/entropy compensation. Regarding the ΔH values for the reaction of **AuL1** and **AuL2** with HSA, both are significantly exothermic, measuring −82.0 kJ mol^{-1} and −56.0 kJ mol^{-1}, respectively. Fig. 6b highlights the dominance of the enthalpy term for both reactions, indicating that uptake of the Au(III) chelates by HSA is enthalpically driven. Notably, the difference in chirality for the two enantiomeric Au(III) chelates is clearly illustrated by their markedly different ΔH and ΔS values. Specifically, the binding of the 1*S*,2*S* enantiomer to HSA is more exothermic when compared with the 1*R*,2*R* enantiomer. However, the reverse (compensatory) scenario applies for ΔS with the 1*R*,2*R* enantiomer having a somewhat more favourable (though still negative) change in entropy for its reaction with HSA.

The Gibbs–Helmholtz relationship (eqn (5)) graphically confirms the enthalpy-driven uptake of both **AuL1** and **AuL2** by HSA (Fig. 6c, data located in the upper right quadrant) and emphasises the distinctly more favourable heat of reaction for the 1*S*,2*S* enantiomer relative to the 1*R*,2*R* enantiomer. For both **AuL1** and **AuL2**, spontaneity is assured because changes in $\Delta H/\Delta G$ are compensated for by commensurate changes in $T\Delta S/\Delta G$. Because the data set is currently small (two enantiomeric compounds), we compared the $T\Delta S/\Delta G$ and $\Delta H/\Delta G$ values measured for **AuL1** and **AuL2** with three similar achiral metal Schiff base chelates (Fig. S24†). From Fig. S24,† it is clear that the Gibbs–Helmholtz relationship is steadfastly

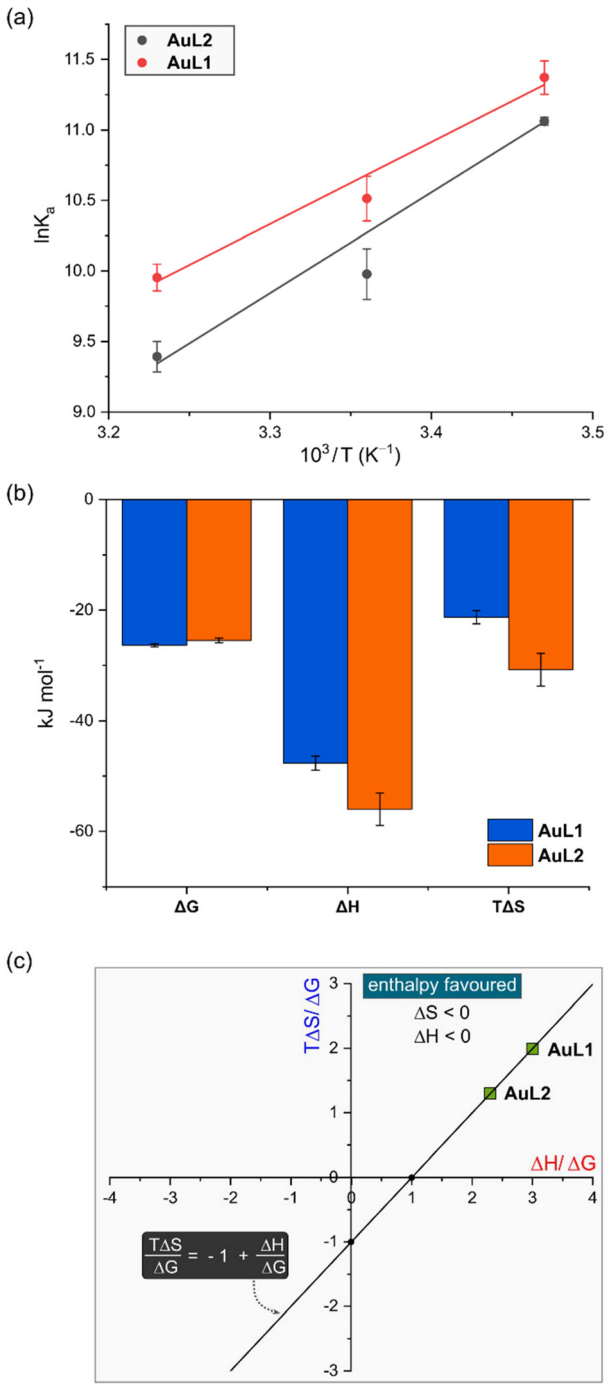

Fig. 6 (a) Linear van't Hoff plots (eqn (4)) for the reactions of **AuL1** and **AuL2** with HSA in 50 mM KH_2PO_4 buffer at pH 7.50. (b) Comparison of the thermodynamic parameters governing the reactions of **AuL1** and **AuL2** with HSA (T = 298 K). (c) All measurements were done in triplicate. Derived parameters were individually averaged. Error bars are estimated uncertainties of the mean for both graphs. (c) Plot of the Gibbs–Helmholtz relationship (eqn (5)) for the reaction of **AuL1** and **AuL2** with HSA at 298 K in 50 mM KH_2PO_4 buffer at pH 7.50. For all reactions, $\Delta G < 0$.

upheld by the current reactions of HSA with related d^8 metal chelates, irrespective of their chirality. Notably, the data yield a defined sequence along the straight-line graph with chelates of the heavier metals tending towards reactions governed by favourable entropy and enthalpy changes (bottom right quadrant: $\Delta H < 0$, $\Delta S > 0$).

Table 3 Thermodynamic parameters for the binding of **AuL1** and **AuL2** by HSA in 50 mM KH_2PO_4 buffer at pH 7.50

Compound	T (K)	ΔG^a (kJ mol^{-1})	ΔH^a (kJ mol^{-1})	ΔS^a (kJ K^{-1} mol^{-1})
AuL1	288	−29.36 (0.1)		
	298	−27.53 (0.1)	−82.0 (3.7)	−0.183 (0.1)
	310	−25.34 (0.2)		
AuL2	288	−26.24 (0.2)		
	298	−25.50 (0.4)	−56.0 (0.3)	−0.103 (0.1)
	310	−23.97 (0.2)		

[a] The estimated standard deviations of the least significant digits are given in parentheses.

The main binding interactions of **AuL1** and **AuL2** with HSA are likely London dispersion forces of attraction since neither **AuL1** nor **AuL2** have typical H-bond donor or acceptor groups; electrostatic interactions involving the cationic complexes will also presumably be feasible. The pyrrole rings may engage in π-type interactions with protein residues, while the bridging cyclohexyl ring would partake in London forces of attraction (hydrophobic interactions).

Fluoroprobe site displacement assays

To determine the preferred binding site(s) for **AuL1** and **AuL2**, we carried out a competitive blocking assay by fluorescence spectroscopy in which both Au(III) chelates were titrated into solutions of native HSA and solutions of HSA that were pre-equilibrated with either warfarin or dansylglycine. From X-ray crystallographic studies, warfarin is known to bind specifically in Sudlow's site I (subdomain IIA).[90] No X-ray structure of HSA bound to dansylglycine has been reported, but dansylglycine has been shown to primarily bind in Sudlow's site II (subdomain IIIA).[91]

Although HSA has numerous drug binding sites,[75] which can complicate interpretation of the data, the idea is that displacement of warfarin from HSA·{warfarin} by the incoming Au(III) chelate (ligand) would signal binding in Sudlow's site I, while displacement of dansylglycine from HSA·{dansylglycine} would suggest uptake of the Au(III) chelate in Sudlow's site II. Complications are anticipated if blocking either Sudlow's site I or II site redirects binding of the incoming Au(III) chelate to an alternative drug binding site within HSA (or hinders its uptake by allosteric inhibition). Despite these potential limitations, changes in the log K_a, n, and K_{SV} values along with displacement of the fluoroprobe itself can help elucidate a possible binding site for the ligand of interest.

AuL1 and **AuL2** (0–9.76 × 10^{-5} M) were titrated into a solution of HSA preequilibrated with either HSA·{warfarin} or HSA·{dansylglycine}. The fluorescence emission spectra of both probe fluorophores are presented in Fig. 7a and b (Fig. S22a and S22b†). The HSA·{warfarin} fluorescence λ_{max}^{em} peaked at 382 nm, which was blue-shifted by 8 nm from that

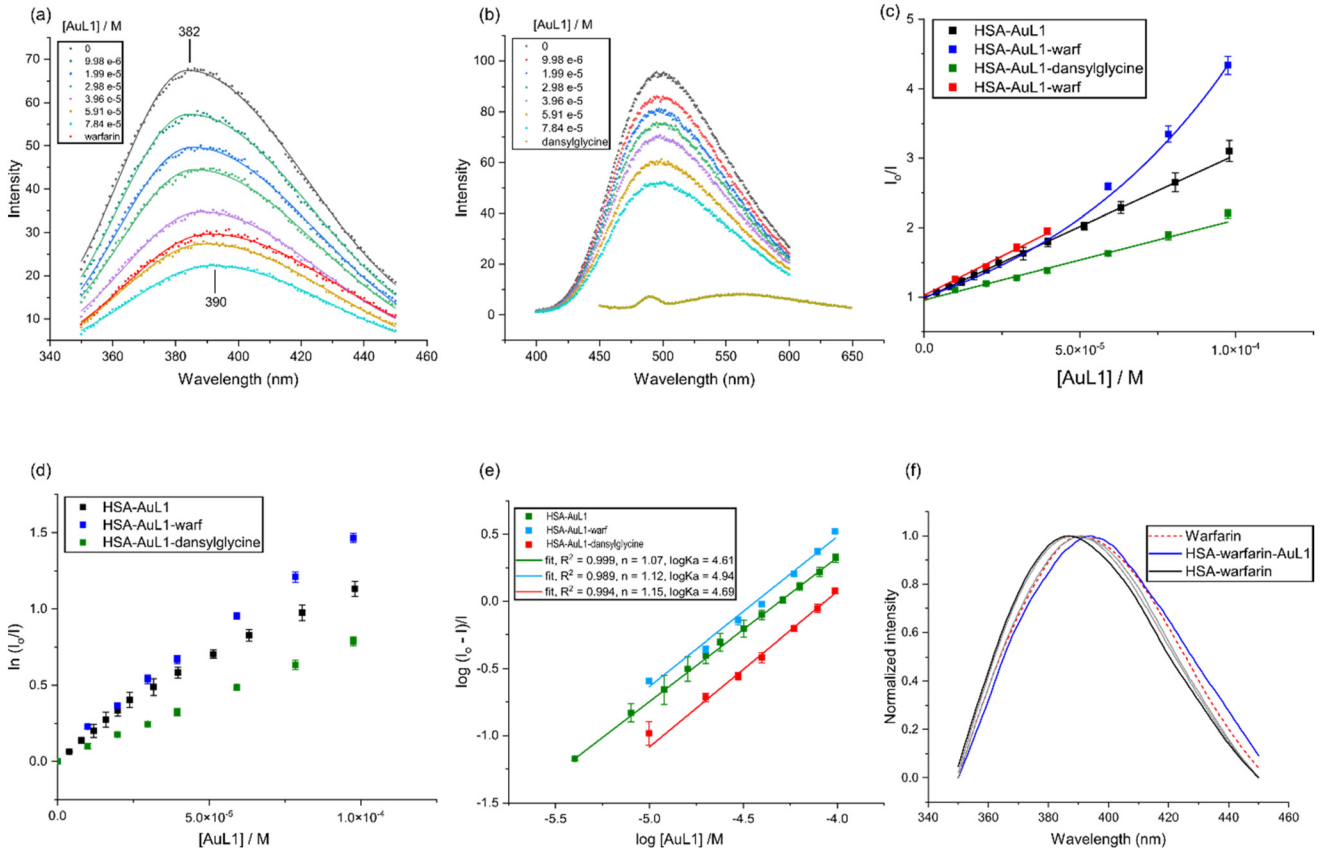

Fig. 7 Binding site determination for the reaction of **AuL1** with HSA (5.0 μM protein, 50 mM KH_2PO_4, pH 7.50, 298 K). (a) Emission spectra of HSA·{warfarin} (5.0 μM warfarin λ^{ex} = 320 nm) recorded as a function of the concentration of **AuL1** at 298 K. The spectra are fitted by single Gaussian functions to locate the emission maxima. Correlation coefficients, R^2, ranged from 0.990 to 0.999. (b) Emission spectra of HSA·{dansylglycine} (5.0 μM dansylglycine λ^{ex} = 340 nm) recorded as a function of the concentration of **AuL1** at 298 K. The spectra are fitted by single Gaussian functions to locate the emission maxima. Correlation coefficients, R^2, ranged from 0.990 to 0.999. (c) Stern–Volmer (SV) plot for native HSA, HSA·{warfarin}, and HSA·{dansylglycine} as a function of the concentration of **AuL1** at 298 K. The plots are linear with an intercept of 1.0 when static quenching is operative (*i.e.*, the quencher binds to the target protein and fluorophore(s)). The excitation and emission wavelengths for the fluorophore probes were: (i) Trp-214 (native HSA), λ^{ex} = 295 nm, λ^{em} = 340 nm; (ii) warfarin (HSA·{warfarin}), λ^{ex} = 320 nm, λ^{em} = 382 nm, and (iii) dansylglycine, λ^{ex} = 340 nm, λ^{em} = 500 nm. (d) Sphere of action model plot, $\ln\left(\frac{I_0}{I}\right) = K_{SV}^{app}[Q]$, for the system. A linear plot with a zero intercept indicates static quenching by **AuL1** bound in some way to the fluorophore/macromolecule. Negative deviation from linearity signals a switch from static to dynamic quenching. (e) Double-log plot (eqn (4)) of the fluorescence quenching data, $\log\left(\frac{I_0-I}{I}\right) = \log K + n\log[Q]$, to enable measurement of $\log K_a$ and the reaction stoichiometry (n). (f) Normalised fluorescence emission spectrum of HSA···warfarin (5.0 μM warfarin λ^{ex} = 320 nm) recorded as a function of the concentration of **AuL1** at 298 K to show the displacement of warfarin from HSA. Error bars indicate the standard deviation of three independent experiments.

of free warfarin (λ_{max}^{em} = 390 nm). Titration of **AuL1** and **AuL2** into the HSA·{warfarin} solution resulted in a monotonic decrease in fluorescence intensity with increasing ligand dose (Fig. 7a and S22a†). The percentage displacement of warfarin is presented Fig. S23.† Further evidence of warfarin being displaced from HSA is the redshift of the warfarin fluorescence emission peak from 382 nm (HSA·{warfarin}) to 390 nm (free warfarin emission peak).

The HSA·{dansylglycine} fluorescence λ_{max}^{em} peaked at 500 nm, which was redshifted 58 nm from that of free dansylglycine (λ_{max}^{em} 558 nm). Titration of **AuL1** and **AuL2** into the HSA·{dansylglycine} solution resulted in a monotonic decrease in fluorescence intensity with increasing ligand dose (Fig. 7b and Fig. S22b†). The suspected percentage displacement of dansylglycine is presented Fig. S23.† Unlike the fluorescence emission spectrum of HSA·{warfarin}, there is no peak shift of HSA·{dansylglycine} to free dansylglycine to suggest dansylglycine is being displaced from HSA. Quenching of the HSA·{dansylglycine} fluorescence by **AuL1** and **AuL2** could reflect quenching by FRET or changing the microenvironment surrounding the fluorophore (*i.e.*, dansylglycine).

The binding mechanism of the Au(III) cyclohexane chelates to HSA·{warfarin} and HSA·{dansylglycine} were further investigated using the Stern–Volmer equation (eqn (1)), the sphere of action model (eqn (6)) and the double logarithmic plot (eqn (3); Fig. 7c–e and S27c–e†).

The Stern–Volmer (SV) plot for native HSA and HSA·{dansylglycine} was linear throughout. However, the

HSA·{warfarin} SV plot deviated from linearity; the deviation suggests two quenching mechanisms are occurring. We propose the linear portion (40 μM of **AuL1** and **AuL2**) was static quenching of warfarin thereafter, the deviation from linearity is a mechanistic switch from static to dynamic quenching. This results from the displacement of warfarin, which is then quenched by the aqueous KH_2PO_4 buffer. The sphere of action model conveniently interprets the nonlinear Stern–Volmer plot for the current HSA-Au(III) chelate system.[85,92] It invokes the presence of a sphere of a finite volume around Trp-214 in which the probability of the quencher (Q) inducing fluorescence quenching is unity.[83] The "sphere of action model" is described by eqn (6) and (7), where K_{SV}^{app} is the apparent static fluorescence quenching constant.

$$\frac{I_0}{I} = e^{\left(K_{SV}^{app}[Q]\right)} \quad (6)$$

$$\ln\left(\frac{I_0}{I}\right) = K_{SV}^{app}[Q] \quad (7)$$

Our interpretation of the site displacement data for **AuL1** and **AuL2** is that neither chelate displaces dansylglycine from HSA·{dansylglycine}; only warfarin is displaced. However, the presence of either fluorescent probe enhances the binding of both chelates, as indicated by the $\log K_a$ values which increase. **AuL1** $\log K_a$ values increase from 4.55 ± 0.11 (n_{total} = 1.05 ± 0.001) in the native protein to 4.94 ± 0.23 (n_{total} = 1.12 ± 0.04) and 4.69 ± 0.17 (n_{total} = 1.15 ± 0.03) in HSA·{warfarin} and HSA·{dansylglycine}, respectively. Based on the $\log K_a$ and K_{SV} values, both Au(III) cyclohexane-bridged chelates bind to HSA by the same mechanism. One interpretation is that each Au(III) chelate binds to HSA in a subdomain close to dansylglycine to quench its fluorescence (*via* FRET). Therefore, both subdomain IIA and IIIA of the native protein (*i.e.*, half- or fractionally-saturate the two sites so that $n_1 + n_2 = n_{total} = 1.15$). The potential of an Au(III) chelate binding to an alternative site cannot be ruled out and may induce conformational changes to HSA, enhancing the binding affinity. This suggests a classic structural synergistic or allosteric effect (cooperative binding). There are several alternate binding sites known for HSA[75] which are located in subdomains IB (bilirubin[93] and hemin binding site[35]) and IIIB (propofol binding site[94]). If both **AuL1** and **AuL2** bind to subdomain IIIB, which is adjacent to IIIA in the protein, they will facilitate efficient additive quenching of the bound dansylglycine fluorescence by FRET.

Far-UV CD spectroscopy

Conformational changes to the secondary structure of a protein can be determined by far-UV CD spectroscopy due to several structural fingerprint spectral regions (*i.e.*, peptide bonds, aromatic amino acids side chains and disulphide bonds[95]). HSA is an α-helix rich protein (67% composition).[34] In Fig. 8a and S29a† far-UV CD spectroscopy (186–260 nm) was employed to delineate the impact of **AuL1** and **AuL2** on the secondary structure of the protein. The far-UV CD spectrum of native HSA displays α-helix rich protein structure with a typical double minimum at 208 ± 1 nm and 222 ± 1 nm.[96] The 208 nm, 222 nm, and 193 nm bands are assigned to π–π*, n–π*, and π–π* transitions, respectively. All three transitions reflect the amide groups of the peptide backbone.[95,96]

Uptake of **AuL1** and **AuL2** by HSA minimally perturbs the secondary structure of the protein, even though both chelates are bound to HSA with a moderately high affinity (10^5 M^{-1}). The amplitudes of the negative CD bands at 208 nm and 222 nm decrease slightly, indicating minor loss of secondary structure. This is accompanied by a slight decrease of the positive ellipticity maximum at 193 nm.

To quantify the changes in the secondary structure of HSA upon binding of **AuL1** and **AuL2**, we analysed the far-UVCD spectra further using JASCO Spectra Manager™ [70] to calculate the percentage composition of each type of secondary structure element present in the protein-bound adducts (Table S1†). The dominant secondary structure domains are α-helices (~58%) and unordered coils (~31%). The α-helicity of HSA was ~58% but was reduced for the protein in the presence of both **AuL1** (by 4.41%) and **AuL2** (by 3.77%). Interestingly, the solution state secondary structure composition for HSA differs from that of native HSA in the solid state[34] (68.5% α-helix, 0% β-sheet, 9.6% turns, and 21.9% unordered coils; PDB code 1BM0 analysed with BeStSel[97]). However, our solution far-UV CD data are consistent with solution state spectral decompositions reported previously.[98–100]

It is largely accepted that enhanced subdomain mobility and general thermal motion/disorder account for the decrease of α-helicity.[96,101]

Near-UV CD spectroscopy

To explain the conformational changes of the tertiary structure of HSA induced by the Au(III) chelates, we utilised near-UV CD spectroscopy between 250–310 nm (Fig. 8a and Fig. S25†). Typically, the near-UV CD spectra of HSA reveal the fine structure perturbations of Trp (285–300 nm), Tyr (275–285 nm) and Phe (250–270 nm) rich regions in the protein that may accompany ligand binding. Key bands (weak negative ellipticity peaks) for HSA respoding to the uptake of **AuL1** are the minima at 262, 280, and 290 nm, which originate from transitions involving the disulphide bonds and the aromatic amino acids.[102]

The near-UV CD spectra of HSA (Fig. 8 and S25†) in the absence of the Au(III) chelates exhibited a weak peak at 290 nm with fine structure between 290–305 nm due to the Trp-214 residue. Between 275 and 285 nm there is a single peak at 284 nm and a shoulder at 287 nm, likely due to the 18 Tyr residues within HSA. The Phe fingerprint region lies between 255 and 270 nm and indicates a peak at 257 nm. Disulfide bonds within HSA are indicated by the two minima at 262 and 268 nm, and a shoulder at 279 nm,[95,103,104] HSA has 17 disulfide bonds.[34] Phe, Tyr and Trp all have π–π* transitions (^1L_a and ^1L_b) and have the potential to be directly involved in π bonding. Therefore, perturbations within the fine structure spectral range can be ascribed to conformational changes of

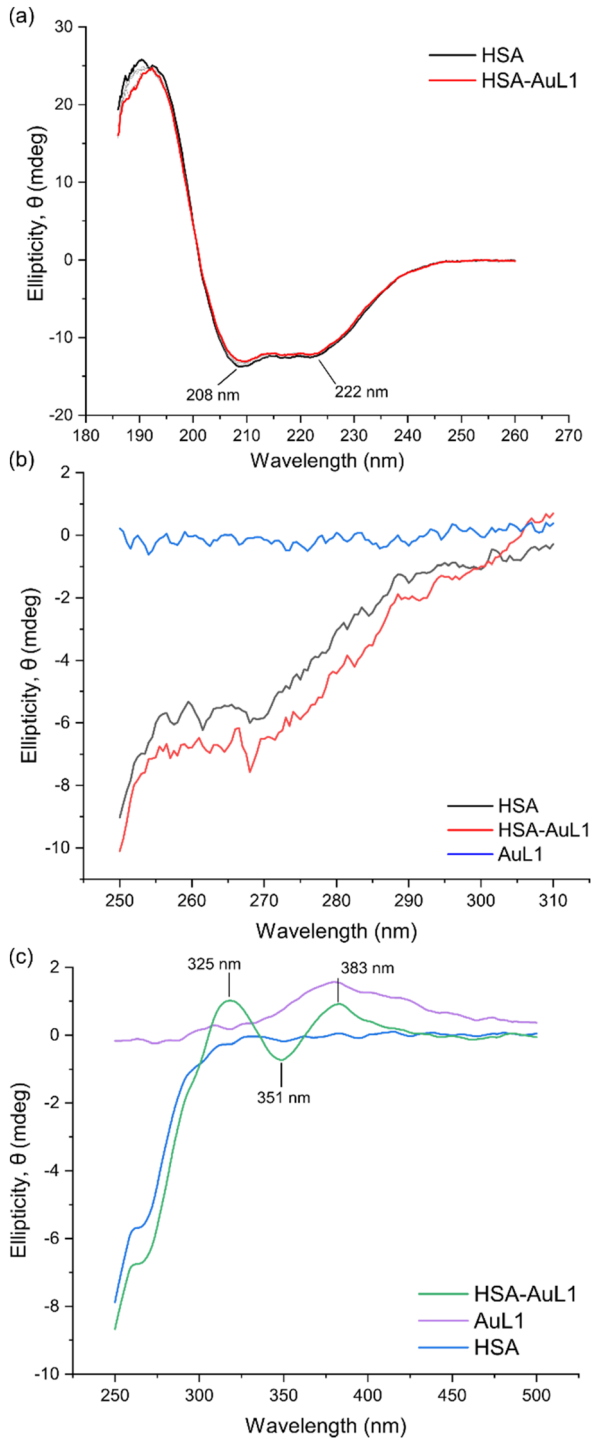

Fig. 8 (a) Plot of the far-UV CD spectra of native HSA (300 nM) and the protein incubated with saturating doses of **AuL1** recorded at 298 K in 50 mM KH_2PO_4 buffer at pH 7.50. The spectra indicate native HSA (black line) and **AuL1** doses ranging from 0.3 μM to 3 μM are grey lines, saturating dose at 6 μM is the red line (Far UV-CD for **AuL2** is given in ESI Fig. S28†). (b) Plot of the near UV-visible CD spectra of native HSA (300 nM) and the protein incubated with a saturating dose (6 μM) of **AuL1**. The spectra were recorded at 298 K in 50 mM KH_2PO_4 buffer at pH 7.50. (c) A plot of the spectra of the HSA·{**AuL1**} complex; it represents the induced CD (ICD) spectrum of the HSA·{**AuL1**} complex. The spectra were smoothed using a Lowess function (0.07 span).

the protein or displacements of the aromatic amino acids, which places them in a different environment.[105]

Both **AuL1** and **AuL2** induced changes to the near-UV CD spectrum of HSA, indicating both chelates bound to the protein in close enough proximity to affect the fine structure around the aromatic amino acid residues. The result was further supported by the site displacement assay (Fig. 7 and S22†) indicating **AuL1** and **AuL2** bound to Sudlow's site I (subdomain IIA containing Trp-214). Furthermore, the 290 nm band had disappeared when **AuL1** bound, however, there was no change in the presence of **AuL2**, further evidence indicating **AuL1** bound closer to Trp-214 than **AuL2**. The 290 nm band has been assigned to the Trp ^1L_b (0,0) band while the 279 nm band was assigned to solvent-exposed Trp in an aqueous solution (^1L_a),[106,107] reflecting HSA conformational changes. There was no significant shift in the disulfide bond fingerprint region, suggesting a negligible change to the bonds. Overall, the binding of **AuL1** and **AuL2** to HSA induced minor conformational changes in both the secondary (Fig. 8a) and tertiary structure (Fig. 8b) of the protein.

Induced CD spectroscopy

Induced circular dichroism (ICD) is a phenomenon by which an achiral molecule binds to a chiral host and acquires a CD signal.[91,108,109] An ICD band has a similar absorbance wavelength as the chromophoric portion of the complex and indicates direct complexation between two molecules, as shown in Fig. 8c. An achiral molecule will exhibit an ICD signal if the symmetry is perturbed and non-zero rotational strengths are formed.[82] Within the scope of this study, both **AuL1** and **AuL2** are chiral and produce intrinsic CD signals (Fig. 8c and S25c†). However, when bound to HSA the UV-vis CD signal of HSA·{**AuL1**} has three peaks, specifically, positive ellipticity maxima at 325 and 383 nm and a negative ellipticity band at 351 nm. The peaks are distinct relative to those for unbound **AuL1**, which has a single, broad positive ellipticity band centred at 382 nm. HSA·{**AuL2**} had a blue shifted peak from 378 nm (free **AuL2**) to 354 nm (protein-bound **AuL2**). Furthermore, a 383 nm peak was present for both **AuL1** and HSA·{**AuL1**}. Finally, HSA·{**AuL1**} was characterized by a distinct new negative ellipticity band at 351 nm (Fig. 8c).

We propose that after the uptake of **AuL1** and **AuL2** by HSA, the protein perturbs the electronic structure of **AuL1** and **AuL2** *via* two mechanisms: (i) intermolecular interactions and (ii) restricting conformational freedom.[109] For an ICD signal, the protein (host) interaction with the small molecule must occur in a preferred orientation that does not allow the ICD signal to be cancelled out. Therefore, ICD is a good indicator of an increase in structure order.[110,111] In Fig. 8c and S25c,† we observe shifts in the ICD bands for the protein-bound complexes relative to the absorbance maxima of the unbound metal chelates. Because the positive ellipticity band at λ ~382 nm in unbound **AuL1** and **AuL2** is retained for HSA·{**AuL1**} and HSA·{**AuL2**}, the Au(III) ion is not reduced to Au(I) after uptake of the chelate by HSA. The ICD spectra there-

fore confirm that both chiral metal chelates bind to HSA as intact Au(III) complexes.

Summary and conclusions

Two Au(III) enantiomers **AuL1** (1*S*,2*S* stereochemistry) and **AuL2** (1*R*,2*R*) chelated by tetradentate cyclohexanediamine-bridged bis(pyrrolide-imine) ligands were synthesized and structurally characterized. **AuL1** and **AuL2** displayed unique mean growth percentages of 56.5% and 89.1%, respectively, in an NCI-60 1-dose screen against 60 human cancer cell lines. A subsequent five-dose NCI-60 screen for **AuL1** afforded mean GI_{50}, IC_{50} and LC_{50} values of 4.7, 4.3, and 39.8 μM, respectively, commensurate with significant cytotoxicity. Heirarchical cluster analysis of the NCI-60 data for **AuL1** indicated a high correlation of the NCI-60 profile for the Au(III) chelate with the vinca alkaloid vinblastine sulphate, an anti-microtubule drug that inhibits mitosis. Statistically, the data suggest that **AuL1** may target microtubular proteins of the mitotic spindle, which represents a novel mechanism of action for this class of compounds and warrants a mechanistic study going forward.

AuL1 was susceptible to reduction from Au(III) to Au(I) in the presence of glutathione (GSH) *in vitro*, suggesting that the Au(III) chelates could potentially also function as prodrugs *in vivo*. Formation of Au(I) species suggests an affinity for thiol-containing enzymes such as thioredoxin reductase and glutathione reductase. Future work will be required to delineate the mechanism of action of the compounds considering these cellular targets in addition to microtubular proteins.

The interaction of **AuL1** and **AuL2** with human serum albumin (HSA) was investigated by complementary spectroscopic techniques to understand how the chirality of the metal chelates impacts their uptake by the protein. Both Au(III) chelates quenched the intrinsic Trp-214 fluorescence of HSA *via* a dynamic quenching mechanism and gave K_a values typical of small molecules binding to HSA ($\sim 10^4$ M^{-1}). The Stern–Volmer quenching constants (K_{SV}) and K_a values for **AuL1** were greater than those for **AuL2**. The present ligands bind to HSA with *negative* ΔH, ΔG and ΔS values, reflecting a spontaneous enthalpy-driven process governed mainly by van der Waals (London dispersion) forces. $T\Delta S/\Delta G$ and $\Delta H/\Delta G$ for both Au(III) chelates were in the upper right quadrant for a plot of the Gibbs–Helmholtz equation. Both **AuL1** and **AuL2** preferentially bound to Sudlow's site I in HSA, minimally perturbing the protein's secondary structure. The induced CD spectra recorded for the metal chelates bound to HSA confirm uptake of the intact complexes without reductive demetallation or imine group hydrolysis.

Author contributions

O. Q. M., S. S., and M. P. A. conceived the study. S. S. and M. P. A. synthesized and characterized the compounds. S. S. performed the HSA spectroscopy and thermodynamics measurements and analyzed the biophysical data. O. Q. M. and M. P. A. performed the crystallography. All authors analysed data, drew figures, and co-wrote specific parts of the paper with final editing by M. P. A. and O. Q. M. Finally, O. Q. M. directed and secured funding for the research programme.

Conflicts of interest

The authors have no conflicts to declare.

Acknowledgements

This work is based on research supported by the South African Research Chairs Initiative of the Department of Science and Innovation (DSI) and National Research Foundation (NRF) of South Africa (Grant No 64799, O. Q. M.). The authors thank WITS University and the NRF for funding to purchase a JASCO J-1500 MCD spectrometer (Grant No 116177, O. Q. M.) and a dual-wavelength Bruker D8 Venture X-ray diffractometer (Grant No 129920, O. Q. M.). We also thank the Centre for High Performance Computing (Project CHEM1065, CHPC, Cape Town) for both the CPU time and resources needed for the DFT simulations. The authors would also like to thank Manuel Fernandes for his expertise in small molecule crystallography. The authors thank the National Cancer Institute Developmental Therapeutics Program (NCI-DTP, USA) for screening **AuL1** and **AuL2**.

References

1 H. Sung, J. Ferlay, R. L. Siegel, M. Laversanne, I. Soerjomataram, A. Jemal and F. Bray, *Ca-Cancer J. Clin.*, 2021, **71**, 209–249.
2 E. J. Anthony, E. M. Bolitho, H. E. Bridgewater, O. W. Carter, J. M. Donnelly, C. Imberti, E. C. Lant, F. Lermyte, R. J. Needham and M. Palau, *Chem. Sci.*, 2020, **11**, 12888–12917.
3 A. Frei, A. G. Elliott, A. Kan, H. Dinh, S. Bräse, A. E. Bruce, M. R. Bruce, F. Chen, D. Humaidy, N. Jung, A. P. King, P. G. Lye, H. K. Maliszewska, A. M. Mansour, D. Matiadis, M. P. Muñoz, T.-Y. Pai, S. Pokhrel, P. J. Sadler, M. Sagnou, M. Taylor, J. J. Wilson, D. Woods, J. Zuegg, W. Meyer, A. K. Cain, M. A. Cooper and M. A. T. Blaskovich, *JACS Au*, 2022, **2**, 2277–2294.
4 B. Rosenberg, L. Van Camp and T. Krigas, *Nature*, 1965, **205**, 698–699.
5 C. J. Ziegler, A. P. Silverman and S. J. Lippard, *JBIC, J. Biol. Inorg. Chem.*, 2000, **5**, 774–783.
6 L. Kelland, *Expert Opin. Invest. Drugs*, 2007, **16**, 1009–1021.
7 M. J. Hannon, *Pure Appl. Chem.*, 2007, **79**, 2243–2261.
8 T. C. Johnstone, K. Suntharalingam and S. J. Lippard, *Chem. Rev.*, 2016, **116**, 3436–3486.
9 S.-H. Chen and J.-Y. Chang, *Int. J. Mol. Sci.*, 2019, **20**, 4136.

10 L. Amable, *Pharmacol. Res.*, 2016, **106**, 27–36.
11 C. R. Wilson, A. M. Fagenson, W. Ruangpradit, M. T. Muller and O. Q. Munro, *Inorg. Chem.*, 2013, **52**, 7889–7906.
12 K. J. Akerman, A. M. Fagenson, V. Cyril, M. Taylor, M. T. Muller, M. P. Akerman and O. Q. Munro, *J. Am. Chem. Soc.*, 2014, **136**, 5670–5682.
13 D. Van der Westhuizen, C. A. Slabber, M. A. Fernandes, D. F. Joubert, G. Kleinhans, C. J. van der Westhuizen, A. Stander, O. Q. Munro and D. I. Bezuidenhout, *Chem. – Eur. J.*, 2021, **27**, 8295–8307.
14 V. Milacic, D. Chen, L. Ronconi, K. R. Landis-Piwowar, D. Fregona and Q. P. Dou, *Cancer Res.*, 2006, **66**, 10478–10486.
15 G. Marcon, S. Carotti, M. Coronnello, L. Messori, E. Mini, P. Orioli, T. Mazzei, M. A. Cinellu and G. Minghetti, *J. Med. Chem.*, 2002, **45**, 1672–1677.
16 B. Bertrand, M. R. Williams and M. Bochmann, *Chem. – Eur. J.*, 2018, **24**, 11840–11851.
17 A. Casini and L. Messori, *Curr. Top. Med. Chem.*, 2011, **11**, 2647–2660.
18 A. Casini, C. Hartinger, C. Gabbiani, E. Mini, P. J. Dyson, B. K. Keppler and L. Messori, *J. Inorg. Biochem.*, 2008, **102**, 564–575.
19 C. Gabbiani, A. Casini, L. Messori, A. Guerri, M. A. Cinellu, G. Minghetti, M. Corsini, C. Rosani, P. Zanello and M. Arca, *Inorg. Chem.*, 2008, **47**, 2368–2379.
20 C.-M. Che, R. W.-Y. Sun, W.-Y. Yu, C.-B. Ko, N. Zhu and H. Sun, *Chem. Commun.*, 2003, 1718–1719.
21 R. D. Teo, H. B. Gray, P. Lim, J. Termini, E. Domeshek and Z. Gross, *Chem. Commun.*, 2014, **50**, 13789–13792.
22 B. Bertrand, J. Fernandez-Cestau, J. Angulo, M. M. D. Cominetti, Z. A. E. Waller, M. Searcey, M. A. O'Connell and M. Bochmann, *Inorg. Chem.*, 2017, **56**, 5728–5740.
23 L. Messori, F. Abbate, G. Marcon, P. Orioli, M. Fontani, E. Mini, T. Mazzei, S. Carotti, T. O'Connell and P. Zanello, *J. Med. Chem.*, 2000, **43**, 3541–3548.
24 V. Bhardwaj, D. Gumber, V. Abbot, S. Dhiman and P. Sharma, *RSC Adv.*, 2015, **5**, 15233–15266.
25 R. N. Brogden, R. C. Heel, T. M. Speight and G. S. Avery, *Drugs*, 1978, **15**, 429–450.
26 H. D. Langtry and J. A. Balfour, *Drugs*, 1998, **55**, 563–584.
27 M. Atkins, C. A. Jones and P. Kirkpatrick, *Nat. Rev. Drug Discovery*, 2006, **5**, 279–280.
28 S. Hannah, V. M. Lynch, N. Gerasimchuk, D. Magda and J. L. Sessler, *Org. Lett.*, 2001, **3**, 3911–3914.
29 J. L. Sessler, T. D. Mody, G. W. Hemmi and V. Lynch, *Inorg. Chem.*, 1993, **32**, 3175–3187.
30 H. Patel, R. Mick, J. Finlay, T. C. Zhu, E. Rickter, K. A. Cengel, S. B. Malkowicz, S. M. Hahn and T. M. Busch, *Clin. Cancer Res.*, 2008, **14**, 4869–4876.
31 R. Gupta, C. Rodrigues Felix, M. P. Akerman, K. J. Akerman, C. A. Slabber, W. Wang, J. Adams, L. N. Shaw, Y.-C. Tse-Dinh and O. Q. Munro, *Antimicrob. Agents Chemother.*, 2018, **62**, e01696-17.
32 M. P. Akerman, O. Q. Munro, M. Mongane, J. A. van Staden, W. I. Rae, C. J. Bester, B. Marjanovic-Painter, Z. Szucs and J. R. Zeevaart, *J. Labelled Compd. Radiopharm.*, 2013, **56**, 530–535.
33 S. Curry, *Drug Metab. Pharmacokinet.*, 2009, **24**, 342–357.
34 X. M. He and D. C. Carter, *Nature*, 1992, **358**, 209–215.
35 P. A. Zunszain, J. Ghuman, T. Komatsu, E. Tsuchida and S. Curry, *BMC Struct. Biol.*, 2003, **3**, 6.
36 M. Fasano, S. Curry, E. Terreno, M. Galliano, G. Fanali, P. Narciso, S. Notari and P. Ascenzi, *IUBMB Life*, 2005, **57**, 787–796.
37 G. Rabbani and S. N. Ahn, *Int. J. Biol. Macromol.*, 2019, **123**, 979–990.
38 B. A. Chabner, *J. Natl. Cancer Inst.*, 2016, **108**, djv388.
39 S. L. Barnholtz, J. D. Lydon, G. Huang, M. Venkatesh, C. L. Barnes, A. R. Ketring and S. S. Jurisson, *Inorg. Chem.*, 2001, **40**, 972–976.
40 J. D. Dunitz, *ChemBioChem*, 2004, **5**, 614–621.
41 J. A. K. Howard, V. J. Hoy, D. O'Hagan and G. T. Smith, *Tetrahedron*, 1996, **52**, 12613–12622.
42 S. S. Batsanov, *Inorg. Mater.*, 2001, **37**, 871–885.
43 DTP/NCI – PubChem Data Source, **https://pubchem.ncbi.nlm.nih.gov/source/DTP%2FNCI**, (accessed February 22, 2023).
44 H. Takeda, M. Haisa, Y. Naomoto, R. Kawashima, K. Satomoto, T. Yamatuji and N. Tanaka, *Jpn. J. Cancer Res.*, 1999, **90**, 677–684.
45 A. Eastman, in *Cisplatin: Chemistry and Biochemistry of a Leading Anti-cancer Drug*, ed. B. Lippert, Wiley, 1999, pp. 111–134.
46 V. M. Guillem, M. Collado, M. J. Terol, M. J. Calasanz, J. Esteve, M. Gonzalez, C. Sanzo, J. Nomdedeu, P. Bolufer and A. Lluch, *Leukemia*, 2007, **21**, 1413–1422.
47 M.-C. Deley, T. Leblanc, A. Shamsaldin, M.-A. Raquin, B. Lacour, S. Danièle, A. Chompret, J.-M. Cayuela, C. Bayle, A. Bernheim, F. de Vathaire, G. Vassal and C. Hill, *J. Clin. Oncol.*, 2003, **21**, 1074–1081.
48 T. Liljefors, P. Krogsgaard-Larsen and U. Madsen, *Textbook of drug design and discovery*, CRC Press, 2002.
49 J. McConathy and M. J. Owens, *Prim Care Companion J. Clin. Psychiatry*, 2003, **5**, 70.
50 P. Fickers, P.-H. Benetti, Y. Waché, A. Marty, S. Mauersberger, M. S. Smit and J.-M. Nicaud, *FEMS Yeast Res.*, 2005, **5**, 527–543.
51 G. M. Cragg, D. G. Kingston and D. J. Newman, *Anti-cancer agents from natural products*, CRC Press, 2005.
52 O. Q. Munro, K. J. Akerman and P. Akerman, *US Pat.*, US9346832, 2016.
53 V. I. Lushchak, *J. Amino Acids*, 2012, **2012**, e736837.
54 S. Sookai and O. Q. Munro, *ChemistryEurope*, 2023, **1**, e202300012.
55 T. Zou, C. T. Lum, S. S. Y. Chui and C. M. Che, *Angew. Chem., Int. Ed.*, 2013, **52**, 2930–2933.
56 F. Guarra, A. Terenzi, C. Pirker, R. Passannante, D. Baier, E. Zangrando, V. Gómez-Vallejo, T. Biver, C. Gabbiani,

W. Berger, J. Llop and L. Salassa, *Angew. Chem., Int. Ed.*, 2020, **59**, 17130–17136.
57 A. M. Al-Majid, M. I. Choudhary, S. Yousuf, A. Jabeen, R. Imad, K. Javeed, N. N. Shaikh, A. Collado, E. Sioriki, F. Nahra and S. P. Nolan, *ChemistrySelect*, 2017, **2**, 5316–5320.
58 W. Liu, K. Bensdorf, M. Proetto, U. Abram, A. Hagenbach and R. Gust, *J. Med. Chem.*, 2011, **54**, 8605–8615.
59 O. Q. Munro, S. D. Strydom and C. D. Grimmer, *New J. Chem.*, 2004, **28**, 34–42.
60 V. Milacic and Q. P. Dou, *Coord. Chem. Rev.*, 2009, **253**, 1649–1660.
61 A. Bindoli, M. P. Rigobello, G. Scutari, C. Gabbiani, A. Casini and L. Messori, *Coord. Chem. Rev.*, 2009, **253**, 1692–1707.
62 M. M. Mohamed and B. F. Sloane, *Nat. Rev. Cancer*, 2006, **6**, 764–775.
63 S. Urig, K. Fritz-Wolf, R. Réau, C. Herold-Mende, K. Tóth, E. Davioud-Charvet and K. Becker, *Angew. Chem., Int. Ed.*, 2006, **45**, 1881–1886.
64 P. Nguyen, R. T. Awwad, D. D. K. Smart, D. R. Spitz and D. Gius, *Cancer Lett.*, 2006, **236**, 164–174.
65 J. Lu and A. Holmgren, *Antioxid. Redox Signal.*, 2012, **17**, 1738–1747.
66 F. Angelucci, A. A. Sayed, D. L. Williams, G. Boumis, M. Brunori, D. Dimastrogiovanni, A. E. Miele, F. Pauly and A. Bellelli, *J. Biol. Chem.*, 2009, **284**, 28977–28985.
67 A. Ilari, P. Baiocco, L. Messori, A. Fiorillo, A. Boffi, M. Gramiccia, T. Di Muccio and G. Colotti, *Amino Acids*, 2012, **42**, 803–811.
68 J. Costa Pessoa and I. Tomaz, *Curr. Med. Chem.*, 2010, **17**, 3701–3738.
69 T. Bohnert and L.-S. Gan, *J. Pharm. Sci.*, 2013, **102**, 2953–2994.
70 G. Colmenarejo, *Med. Res. Rev.*, 2003, **23**, 275–301.
71 B. Demoro, R. F. M. de Almeida, F. Marques, C. P. Matos, L. Otero, J. C. Pessoa, I. Santos, A. Rodríguez, V. Moreno, J. Lorenzo, D. Gambino and A. I. Tomaz, *Dalton Trans.*, 2013, **42**, 7131–7146.
72 M.-X. Xie, X.-Y. Xu and Y.-D. Wang, *Biochim. Biophys. Acta, Gen. Subj.*, 2005, **1724**, 215–224.
73 T. Peters Jr., *All about albumin: biochemistry, genetics, and medical applications*, Academic Press, 1995.
74 O. K. Abou-Zied and O. I. K. Al-Shihi, *J. Am. Chem. Soc.*, 2008, **130**, 10793–10801.
75 J. Ghuman, P. A. Zunszain, I. Petitpas, A. A. Bhattacharya, M. Otagiri and S. Curry, *J. Mol. Biol.*, 2005, **353**, 38–52.
76 Z.-D. Qi, B. Zhou, X. Qi, S. Chuan, Y. Liu and J. Dai, *J. Photochem. Photobiol., A*, 2008, **193**, 81–88.
77 P. R. Callis, *J. Mol. Struct.*, 2014, **1077**, 22–29.
78 A. Divsalar, M. J. Bagheri, A. A. Saboury, H. Mansoori-Torshizi and M. Amani, *J. Phys. Chem. B*, 2009, **113**, 14035–14042.
79 M. H. Gehlen, *J. Photochem. Photobiol., C*, 2020, **42**, 100338.
80 M. K. Helms, C. E. Petersen, N. V. Bhagavan and D. M. Jameson, *FEBS Lett.*, 1997, **408**, 67–70.
81 K. Flora, J. D. Brennan, G. A. Baker, M. A. Doody and F. V. Bright, *Biophys. J.*, 1998, **75**, 1084–1096.
82 T. K. Maiti, K. S. Ghosh, A. Samanta and S. Dasgupta, *J. Photochem. Photobiol., A*, 2008, **194**, 297–307.
83 S. Soares, N. Mateus and V. de Freitas, *J. Agric. Food Chem.*, 2007, **55**, 6726–6735.
84 G. G. Ariga, P. N. Naik, S. A. Chimatadar and S. T. Nandibewoor, *J. Mol. Struct.*, 2017, **1137**, 485–494.
85 J. R. Lakowicz, *Principles of fluorescence spectroscopy*, Springer, 2006.
86 P. D. Ross and S. Subramanian, *Biochemistry*, 1981, **20**, 3096–3102.
87 H. Yin, L. Liao and J. Fang, *JSM Clin. Oncol. Res.*, 2014, **2**, 1010.
88 C. Lagercrantz, T. Larsson and I. Denfors, *Comp. Biochem. Physiol., C: Comp. Pharmacol.*, 1981, **69**, 375–378.
89 H. Rimac, C. Dufour, Ž. Debeljak, B. Zorc and M. Bojić, *Molecules*, 2017, **22**, 1153.
90 I. Petitpas, A. A. Bhattacharya, S. Twine, M. East and S. Curry, *J. Biol. Chem.*, 2001, **276**, 22804–22809.
91 F. S. Graciani and V. F. Ximenes, *PLoS One*, 2013, **8**, e76849.
92 S. A. C. Lima, A. Cordeiro-da-Silva, B. de Castro and P. Gameiro, *Biophys. Chem.*, 2007, **125**, 143–150.
93 P. A. Zunszain, J. Ghuman, A. F. McDonagh and S. Curry, *J. Mol. Biol.*, 2008, **381**, 394–406.
94 A. A. Bhattacharya, S. Curry and N. P. Franks, *J. Biol. Chem.*, 2000, **275**, 38731–38738.
95 S. M. Kelly, T. J. Jess and N. C. Price, *Biochim. Biophys. Acta, Proteins Proteomics*, 2005, **1751**, 119–139.
96 N. Sreerama and R. W. Woody, in *Methods in Enzymology*, Academic Press, 2004, vol. 383, pp. 318–351.
97 A. Micsonai, F. Wien, É. Bulyáki, J. Kun, É. Moussong, Y.-H. Lee, Y. Goto, M. Réfrégiers and J. Kardos, *Nucleic Acids Res.*, 2018, **46**, W315–W322.
98 F. Mohammadi, A.-K. Bordbar, A. Divsalar, K. Mohammadi and A. A. Saboury, *Protein J.*, 2009, **28**, 189–196.
99 H. A. Tajmir-Riahi, C. N. N'Soukpoe-Kossi and D. Joly, *Spectroscopy*, 2009, **23**, 81–101.
100 O. Duman, S. Tunç and B. Kancı Bozoğlan, *J. Fluoresc.*, 2013, **23**, 659–669.
101 P. Alam, S. K. Chaturvedi, T. Anwar, M. K. Siddiqi, M. R. Ajmal, G. Badr, M. H. Mahmoud and R. Hasan Khan, *J. Lumin.*, 2015, **164**, 123–130.
102 D. Lafitte, P. O. Tsvetkov, F. Devred, R. Toci, F. Barras, C. Briand, A. A. Makarov and J. Haiech, *Biochim. Biophys. Acta, Proteins Proteomics*, 2002, **1600**, 105–110.
103 B. Ahmad, S. Parveen and R. H. Khan, *Biomacromolecules*, 2006, **7**, 1350–1356.
104 C. Sun, J. Yang, X. Wu, X. Huang, F. Wang and S. Liu, *Biophys. J.*, 2005, **88**, 3518–3524.

105 X.-X. Cheng, X.-Y. Fan, F.-L. Jiang, Y. Liu and K.-L. Lei, *Luminescence*, 2015, **30**, 1026–1033.
106 A. Barth, S. R. Martin and P. M. Bayley, *Biopolym. Orig. Res. Biomol.*, 1998, **45**, 493–501.
107 B. Valeur and G. Weber, *Photochem. Photobiol.*, 1977, **25**, 441–444.
108 S. Allenmark, *Chirality*, 2003, **15**, 409–422.
109 D. Tedesco and C. Bertucci, *J. Pharm. Biomed. Anal.*, 2015, **113**, 34–42.
110 G. Gottarelli, S. Lena, S. Masiero, S. Pieraccini and G. P. Spada, *Chirality*, 2008, **20**, 471–485.
111 G. Pescitelli, L. D. Bari and N. Berova, *Chem. Soc. Rev.*, 2014, **43**, 5211–5233.